Chemical Engineering Science 176 (2018) 503–514

Contents lists available at ScienceDirect

Chemical Engineering Science

journal homepage: www.elsevier.com/locate/ces

Transport characteristics of saturated gas diffusion layers treated with hydrophobic coatings

Seyed Mohamad Moosavi [a], Mathias Niffeler [a], Jeff Gostick [b], Sophia Haussener [a,*]

[a] Institute of Mechanical Engineering, École Polytechnique Fédérale de Lausanne, 1015 Lausanne, Switzerland
[b] Department of Chemical Engineering, University of Waterloo, Waterloo, ON, Canada

HIGHLIGHTS

- In-situ X-ray computed tomography to characterize saturated GDL samples.
- Surface coating rises rel. eff. permeability and GDL's water removal performance.
- Importance of phase connectivity and percolation is demonstrated.
- Direct pore-level simulation provides direct insight on flow paths and tortuosity.

ARTICLE INFO

Article history:
Received 25 June 2017
Received in revised form 19 October 2017
Accepted 23 October 2017
Available online 27 October 2017

Keywords:
Fuel cell
Gas diffusion media
Permeability
Morphological characterization

ABSTRACT

Water flooding of cathodic gas diffusion layers (GDLs) in proton-exchange membrane fuel cells at high current densities or low temperatures limits efficient operation due to disturbed transport of reactants to the catalytic sites or products away into the channels. We utilize tomography-based direct pore-level simulations to provide quantitative insights into the transport characteristics of partially saturated GDLs with and without hydrophobic surface treatment to eventually guide the design of better GDLs. High-resolution (voxel size of 1.3 μm) computed tomography images of two different types commercial Toray TGP-H-120 GDLs, one of them untreated and the other treated by hydrophobic coatings, at different water saturation levels were taken. These images were then digitally processed to precisely segment the gas, water, and fiber phases. The digitalized phase information was used in direct pore-level numerical flow simulations to determine effective relative diffusivity of the gas phase, relative permeability of the gas and liquid water phases, and tortuosity in the gas phase. Mathematical morphology operations were used to calculate size distributions of the liquid water phase and the gas phase at different saturation levels for a better understanding of the pore occupation by water at different capillary pressure. Percolation simulations were used to provide information on the connectivity of the gas and liquid phases. The results were validated with reported experimental data and semi-empirical correlations. Power law expressions provide a good level of accuracy for curve fitting. The hydrophobic coating does not affect the relative permeability and effective realtive diffusivity of air; however, it improves the water permeability significantly. The quantitative results presented provide insights and guidance for designing GDLs with better transport behavior.

1. Introduction

Proton-exchange-membrane fuel cells (PEMFCs) have shown their potential as a new energy conversion system in a variety of applications. They have been favored over other types of fuel cells since they are efficient, portable and environmental friendly. However, their high production costs, limited durability and some technological limitations still prevent them from being commercialized. A PEMFC is composed of catalyst layers on both anode and cathode sides, a proton conducting membrane, gas diffusion layers (GDLs) on each side, and gas channels for feeding the reactants and removing the products. Significant limitations for performance are effective heat removal and transport limitations in the GDLs, especially at high operating current densities.

GDLs play an important role in PEMFCs. Their functions can be categorized in three main tasks; transferring chemical reactants from the gas channel to the catalyst layer especially to the regions

* Corresponding author.
E-mail address: sophia.haussener@epfl.ch (S. Haussener).

https://doi.org/10.1016/j.ces.2017.10.035
0009-2509/

Nomenclature

A_o	specific surface area [m^2]
c	local concentration [kg m^{-3}]
d	diameter [m]
D	bulk diffusion coefficient [m^2 s^{-1}]
f	relative effective diffusivity function for porosity contribution, and frequency distribution
g	relative effective diffusivity function for saturation contribution
k	permeability [m^2]
$k_{r,i}$	relative permeability of phase i
l	length [m]
l^*	minimum edge length of REV [m]
m	empirical exponent factor
n	empirical exponent factor
p	pressure
Per	Percolation index [fraction]
$\mathbf{r}$	position vector for spatial coordinates in the sample [m]
r	distance between two points in the sample [m]
REV	representative elementary volume [m^3]
$\mathbf{s}$	vector of path direction [m]
s	saturation, and path length [m]
s_2	two-point correlation function
u	local velocity [m s^{-1}]
$\overline{u_D}$	superficial velocity (Darcean velocity) [m s^{-1}]
V	sample volume [m^3]
z	through plane axes direction [m]

Greek symbols

α	empirical exponent factor, and threshold value for segmentation
β	empirical exponent factor
γ	surface tension [N m^{-1}]
Λ	local connectivity indicator
δ	convergence threshold of REV [percent volume fraction]
ε	porosity (air volume over total sample's volume)
θ	three phase contact angle [rad]
λ	empirical exponent factor
μ	dynamic viscosity [Pa s]
τ	tortuosity
ψ	pore scale indicator function
Ω	solid angle [sr]

Subscripts

a	air
c	capillary
w	liquid water
op	opening

Superscript

eff	effective
$\widehat{\ }$	unit vector

under the ribs, heat conduction and electron delivery from the catalyst layer to the bi-polar plate, and transferring reaction products to the gas channels (Larminie et al., 2003). Gas diffusion media, which are porous structures made from carbon fibers, are used for this application. The porous structure of a gas diffusion medium enables transport of the reactants and the reaction products through the pores, while the electrons are transferred in the highly conductive carbon fibers. The reaction product of the cell, water, condenses into liquid at low temperatures or high current densities. The liquid phase hinders the transport of gaseous reactants through the pores by partially occupying the available pore passages. This phenomenon is called GDL flooding and it decreases the cell's performance dramatically. Consequently, optimal water management in GDLs is crucial to ensure acceptable performance of the cell at high operating currents and durable cell performance (Larminie et al., 2003; Wang, 2004; Weber and Newman, 2004).

To avoid water flooding in a GDL, the gas diffusion medium can be treated by hydrophobic coatings such as polytetrafluoroethylene (PTFE). A thin layer of hydrophobic PTFE wet proofs the carbon fibers to enhance water management. On the other hand, adding large weight percentages of PTFE reduces the porosity of the gas diffusion media (Rashapov et al., 2015), which results in difficulties for reactants transportation and higher electrical and thermal contact resistances. Additionally, the surface coating changes the surface properties of the fibers affecting pressure losses in the media or degradation (Kumar et al., 2012; Park et al., 2015; Yu et al., 2014). Thus, an optimal PTFE loading should be used to improve performance of the cell (Fishman and Bazylak, 2011; LaManna and Kandlikar, 2011). Understanding the effects of water flooding and PTFE loading on transport properties of gas diffusion media is essential to design and optimize the PEMFCs' GDL and working conditions. The characterization of transport properties of gas diffusion media has attracted attention and has been reviewed (Weber and Newman, 2004; Zamel and Li, 2013). However, to date no thorough study has been performed comparing the multi-physical transport in saturated GDLs with and without PTFE using direct pore-level simulations utilizing the exact morphology obtained by X-ray tomography, and simultaneously comparing and explaining these results by utilizing detailed and quantitative morphology and percolation analyses.

The numerical study of transport processes directly on microstructural images is a powerful approach that provides estimates of transport parameters without performing complicated and difficult experiments. The availability of high power computing and advanced X-ray imaging beamlines provides the opportunity for high-resolution imaging and simulations. One limitation of this approach is the difficulty of simulating water phase distributions. Some techniques such as level sets (Prodanović and Bryant, 2006) or morphological image opening (Hilpert and Miller, 2001) only allow perfectly wetting fluids; other approaches such as multiphase Lattice-Boltzmann, which include surface energy differences, are computationally very intensive. The most reliable means of obtaining realistic invading water configurations is to physically inject water into the sample during non-intrusive 3D imaging, as was done in the present work. The impact of hydrophobic polymer treatments on multiphase transport parameters can then be assessed by performing numerical simulations of diffusion and flow in images of different materials.

The determination of these parameters is traditionally performed experimentally, and there are numerous reports for GDLs in the literature. Most of these studies are limited to dry samples which have revealed strong correlations of the transport properties to porosity, pores structure, sample thickness, and PTFE loading (Chan et al., 2012; Flückiger et al., 2008; LaManna and Kandlikar, 2011; Rashapov and Gostick, 2016). Recently, Rashapov et al. made extensive measurements of the in-plane diffusivity as a function of compression and PTFE loading, both of which decrease the porosity (Rashapov and Gostick, 2016). They found that the tortuosity of the

samples increases significantly as porosity drops. Büchi and coworkers employed electrochemical diffusimetry to measure the through-plane effective diffusivity in dry gas diffusion media samples with different levels of wet proofing and compression (Flückiger et al., 2008; Kramer et al., 2008), and also noted a strong increase in tortuosity. These experimental results are valuable, but time consuming and challenging. Experiments on partially water filled samples are even more difficult to perform, with only a few reports available. Utaka et al. studied the effect of different wet proofing strategies on gas diffusivity for partially water saturated samples (Utaka et al., 2009). An ex-situ electrochemical limiting-current method was used by Hwang and Weber (2012) to measure effective diffusivity in commercial gas diffusion media at various water saturations.

For relative permeability of air and water through gas diffusion media, there is less data in the literature as it is challenging to maintain a stagnant water phase and/or control the saturation. Hussaini et al. measured the relative permeability of gas diffusion layers by an ex-situ gravimetric method (Hussaini and Wang, 2010). Several groups have used direct numerical simulation to estimate the relative permeability. Koido et al. used the Lattice-Boltzmann method to numerically investigate the relative permeability (Koido et al., 2008). Direct solution of the Navier-Stokes equations (at very low Re numbers) in the complex flow domain has also been used, were the simulation domain was reconstructed from tomographic images or artificially generated fiber media (Rosén et al., 2012; Zamel et al., 2011). Rosén et al. used the Lattice-Boltzmann method to simulate flow in a partially saturated Toray TGP-H-60, showing good agreement with experimental data (Rosén et al., 2012). Pore network modelling has also been used for the calculation of diffusivity and permeability in porous materials, and has been used to study GDLs (Ghanbarian and Cheng, 2016; Gostick et al., 2007; Ismail et al., 2015). The effect of PTFE on relative permeability was not reported in the literature, with the exception of a short comment by Sole (Sole, 2008).

Here, we combine computed tomography with direct pore-level numerical fluid flow simulations in partially saturated gas diffusion media to estimate transport properties at different levels of saturation and PTFE loading. This approach has been developed and successfully tested for the transport characterization in morphologically-complex two-phase media (Haussener et al., 2010, 2012; Suter et al., 2014). In contrast to previous investigations of transport in GDLs, we use finite volume methods for the calculation providing benefit in computational speed and accuracy. We use in-situ computed tomography to obtain the exact morphology of the fibers and liquid water distribution for different saturations, both to be incorporated in the numerical simulations. We derive power law expressions with variable exponent factors, widely used in literature for the quantification of relative permeability and effective relative diffusivity of gas diffusion media (Hussaini and Wang, 2010; Hwang and Weber, 2012; Koido et al., 2008; Martínez et al., 2009; Nam and Kaviany, 2003; Nguyen et al., 2006; Rosén et al., 2012), to quantify and validate our modeling results. We provide consistent data for effective relative diffusivity and relative permeability using the same computational method and the same samples. For the first time, we report on results for bare and PTFE-loaded GDL samples as well as on results obtained from calculations in the gas and liquid phases of the pore space. Furthermore, we use mathematical morphology operations to provide quantitative morphological characterization of the gas phase and the liquid water phase as a function of the saturation (or capillary pressure) in the GDL. Additionally, percolation calculations are performed to demonstrate the difference between the percolation of different phases. These combined analyses allow for a better understanding of the physics behind the transport processes, aiming at guiding the design of better GDL materials. The direct pore-level simulations (DPLSs) enable us to calculate tortuosity directly from the flow field, which provides an alternative way to predict the effective diffusivity. The direct calculation of diffusivity and the tortuosity-based diffusivity calculations will be compared.

2. Theory and methodology

2.1. Materials

Commercial gas diffusion layers Toray-TGP-H-120 with and without PTFE loading, namely 0 wt-% (series A) and 10 wt-% (series C) were investigated. The PTFE loadings were provided by the manufacturer. The GDLs were 375 μm-thick and 3.2 mm diameter carbon papers composed of carbon fibers with diameters of around 10 μm.

2.2. Experimentation and in-situ tomography

In-situ X-ray computed tomography (CT) of the GDL under different liquid water saturation operation was obtained at the beamline 8.3.2, a synchrotron-based Hard X-ray Micro-Tomography instrument, of the Advanced Light Source at the Lawrence Berkeley National Lab with high resolution and voxel size of 1.3 μm. The sample holder is shown in Fig. 1a. It consisted of a 20 mm diameter PTFE holder, bored through with a 3.2 mm ID hole as sample holder. The sample was positioned in a section of the rod which was turned down to 4.2 mm OD (0.5 mm thickness) to reduce the X-ray attenuation. A PTFE tube was inserted from the bottom into the holder and held in place by a friction fit. This tube acted as the sample stage. The tube extended away from the holder by several meters and was connected to an elevated water reservoir, the height of which was used to control the applied capillary pressure to the GDL sample sitting on the tube outlet. Above the sample, a second piece of PTFE tubing was inserted, also by friction fit. The end of this second tube was blocked by a PTFE membrane (220 nm pores, Sartorius), which allowed air to escape the sample as water invaded, but prevented water from leaving the system, thereby allowing capillary pressures and saturations beyond the breakthrough point to be studied. Evaporated water could escape the system together with the air, however, the evaporated water was replenished as the setup was pressure controlled and water flew in as needed. The liquid water saturation, s, represents the volume fraction of the pore volume of the dry GDL occupied by liquid water. The capillary pressure (p_c), i.e. the difference between two pressures of the two phases (p_a and p_w), relates the three-phase contact angle, surface tension (γ) between water and air, and the pore radius (r),

$$p_c = p_a - p_w = \frac{2\gamma\cos\theta}{r}. \quad (1)$$

Capillary pressure was varied by raising the water head above the sample in 10 cm increments (~1000 Pa), corresponding to capillary pressures of 0–6000 Pa and 0–8000 Pa for the series A and series C samples, respectively, covering a wide range of saturations from dry to fully saturated samples.

Tomographic images were obtained by collecting 1080 radiographs over 180° of rotation at each applied capillary pressure. The exposure time for each radiograph was 100 ms, for a total scan time of less than 2 min. These values were chosen since they produced excellent quality reconstructions while minimizing the scan time. Shorter scans led to noticeably higher noise, which was problematic for segmentation of the three coexisting phases. Reconstructions were performed using the commercial software Octopus. It was found that in order to produce useable images,

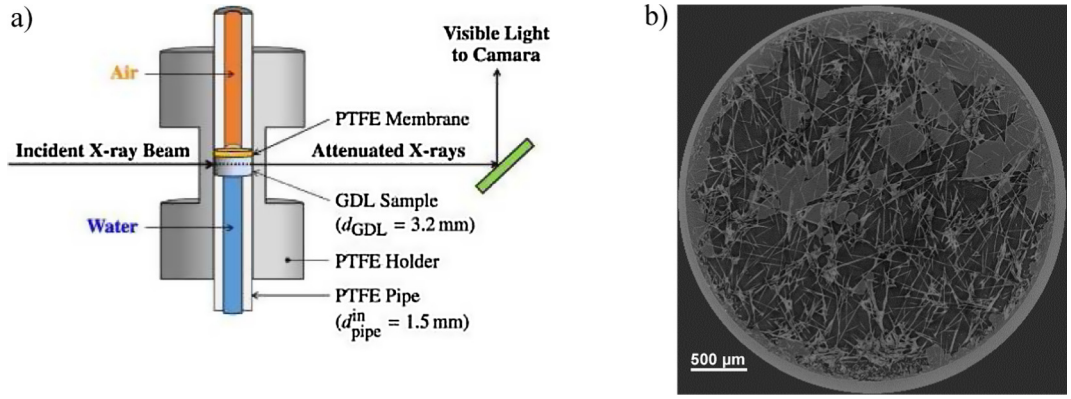

Fig. 1. (a) Schematic diagram of the sample holder used for the in-situ X-ray tomography (Reprinted from García-Salaberri et al. (2015b). Effective diffusivity in partially-saturated carbon-fiber gas diffusion layers: effect of through-plane saturation distribution, Int. J. Heat Mass Transf. 86, 319–333., Copyright 2017, with permission from Elsevier.), and (b) an example 2D cut through a CT-image of the A-series sample with water saturation at a capillary pressure of 4000 Pa. Each image slice has one voxel thickness, i.e. 1.3 µm.

phase contrast mode was necessary rather than absorption contrast mode (Flückiger et al., 2011). Accordingly, imaging was performed at 32 keV, and a modified Bronnikov filter (available in Octopus) was applied to enhance the phase contrast in each radiograph. An example of a slice through a reconstructed sample is depicted in Fig. 1b.

To choose the simulation domain size, we performed representative elementary volume (REV) analysis to find the smallest sample volume for which continuum assumptions are still valid. The definition of REV varies (Bear and Bachmat, 1990; Rosén et al., 2012). Here, we selected REV based on convergence of each phases' volume fraction. The volume fraction for each phase was calculated for sub-volumes with increasing volume size until it varied only within a band of ±δ (Petrasch et al., 2008), chosen equal to 2%. REV analysis showed that the minimum required volume was between 0.2 and 0.3 mm^3 (dependent on saturation) for convergence of phases' volume fraction. Eventually, the largest possible sample sizes were chosen as computational domain, centered in the physical sample and cut off the edges to remove edge effects (García-Salaberri et al., 2015a), such as the outer diameters of the cylindrical sample holder and the regions close to the physical water and air inlet and exit. The resulting samples sizes were $1170 \times 1170 \times 260$ μm^3 and $1170 \times 1170 \times 247$ μm^3, respectively, for series A and series C samples. Indeed, these samples with volume of 0.35 mm^3 and 0.34 mm^3 for sample A and C, respectively, satisfied the per REV analysis required conditions.

2.3. Phase segmentation and digitalization

The collected CT data was further digitally processed for subsequent phase segmentation to reconstruct the three individual phases, namely the solid fibers, the liquid water, and the gas-filled void phase. There are various image processing techniques available in literature for segmentation of CT images and their accuracy varies from case to case (Jain, 1989; Kaestner et al., 2008; Wildenschild and Sheppard, 2013). Histogram-based segmentation such as the mode method has been commonly used for segmentation (Gonzalez and Woods, 2002; Weszka, 1978) and has successfully been applied for complete heat and mass transport characterization and pore-optimization of porous ceramics (Suter et al., 2014).

Segmentation becomes more challenging in three phase media. Rosén et. al. used hole/island removal method with manual correction for the analysis of saturated GDLs (Rosén et al., 2012). In our study, we obtained the most accurate segmentation, with regards to visual inspection and comparison to experimental porosities, by using an anisotropic diffusion filter in 3D (Perona and Malik, 1990) followed by thresholding. The filter parameters used for the anisotropic diffusion filters were 4 for diffusion coefficient, 0.07 s for time step and 30 iterations in each direction. These values were chosen by varying and tuning each parameter in a wide range. This method was applied to the dry (two phase samples) for the segmentation of pore space and fibers utilizing threshold value $\alpha_{t,1}$. Since the intensity of water and fibers is similar, intensity-based segmentation methods failed to correctly identify and separate these two phases. Here, by assuming the fibers retain their geometry and location for changing saturation, we used the segmented dry samples to remove the fiber from the saturated samples. This was done by manually aligning the dry sample to the wet samples, followed by subtraction of the fibers from the saturated sample. Subsequently a threshold-based segmentation (utilizing $\alpha_{t,2}$) was used to identify and separate the water and gas phases. The noise in the remaining fiber-free sample was reduced by applying a set of filters, including erosion and median filters. Eventually, to compensate the eroded water voxels, closing and dilation filters were applied on the samples (Fig. 2). The sensitivity of the results on the chosen thresholds ($\alpha_{t,1}$ and $\alpha_{t,2}$) was investigated by comparing the calculated gas phase volume fraction and saturation for thresholds varying within ±5%. The variation in the volume fraction stayed within +3% and −2%, and the saturation within −2% and +1%. The saturation showed higher sensitivity towards $\alpha_{t,2}$ than $\alpha_{t,1}$. The variation of the effective diffusivity stayed within −6% and +7%, and the effective relative diffusivity stayed within −8% and 9% (for sample A at p_c = 5 kPa). The effective relative diffusivity showed higher sensitivity towards $\alpha_{t,1}$ than $\alpha_{t,2}$.

2.4. Morphological characterization

Quantified characterization of the morphology of different phases in saturated GDLs provides basis for the understanding on transport properties of complex porous materials. This characterization includes determination of pore volume fraction, specific surface area, size distribution, and percolation analysis of the three segmented phases in the previous step.

The discrete morphology of a sample can be described by a matrix $\psi(\mathbf{r})$, where the value of ψ at a location $\mathbf{r}$ indicates the phase by an integer number. The properties of the two point correlation function can be used to determine pore volume fraction, f_v, and specific surface area, A_0, of the various phases by employing the following set of equations (Berryman and Blair, 1986),

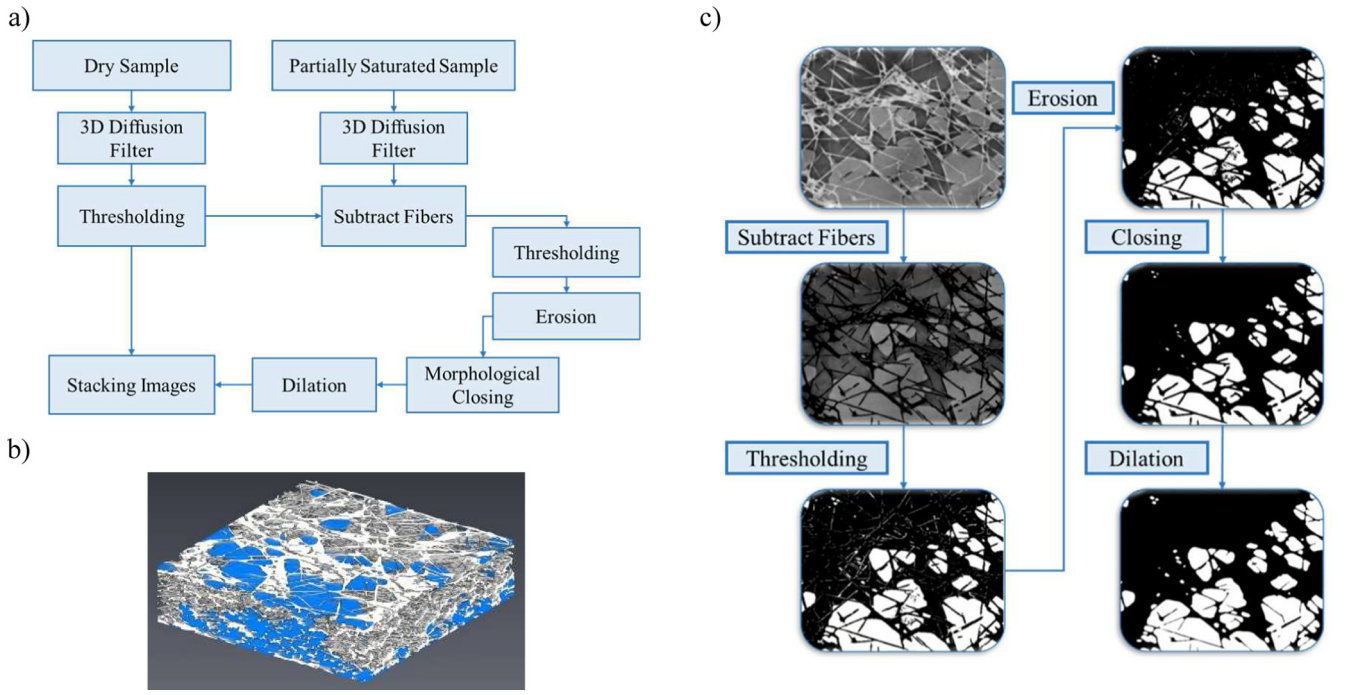

Fig. 2. (a) Flowchart representation of the image processing steps implemented for the phase segmentation of the CT-images, (b) 3D rendering of reconstructed sample C ($1170 \times 1170 \times 247\ \mu m^3$), and (c) example slice to which the processing steps are applied for the liquid phase segmentation.

$$s_2(r) = \frac{\int_V \int_{4\pi} \psi(\mathbf{r})\psi(\mathbf{r}+r\hat{\mathbf{s}})d\Omega dV}{4\pi V}, \tag{2}$$

$$s_2(r=0) = f_v, \tag{3}$$

$$\left.\frac{ds_2}{dr}\right|_{r=0} = -\frac{A_0}{4}. \tag{4}$$

The two-point correlation functions were determined by Monte Carlo sampling. The phase size distribution was determined by using mathematical morphology operations, specifically opening operations using spherical structuring elements with diameter d. The volume fraction of the phase after an opening with such a spherical element, $f_{v,\mathrm{op}}(d)$, can be used to calculate the phase size distribution function (Haralick et al., 1987)

$$f(d) = -\frac{\mathrm{d}f_{v,\mathrm{op}}(d)}{f_v \mathrm{d}d}. \tag{5}$$

This size distribution represents the size of the smallest dimension of a connected 3D object (for example for a cylinder, the opening distribution size would be its radius).

To quantify the connectivity of each phase and assess their percolation, a local connectivity indicator function from local porosity theory (Hilfer, 1996) was computed for sub volumes of the sample,

$$\Lambda_i = \begin{cases} 1 & \text{if cell } i \text{ is percolating} \\ 0 & \text{otherwise} \end{cases}. \tag{6}$$

A cell is percolating in a direction if the two opposite boundary faces perpendicular to the direction are connected via a path through the corresponding phase. Knowing the local connectivity indicator of the sample, the total fraction of percolation of the sample can be obtained:

$$\mathrm{Per} = \frac{1}{N}\sum_{i=1}^{N}\Lambda_i. \tag{7}$$

2.5. Mass transfer

The characterization of the pressure loss and the concentration gradient along a GDL sample are given by the (relative) permeability and the effective (relative) diffusivity. These quantities are homogenized (also called volume-averaged) quantities which provide a macroscopic description of these microscopic phenomena (Whitaker, 1999). Macroscopically, Darcy's law (Darcy, 1856)

$$\nabla p = -\frac{\mu}{\mathbf{k}}\bar{\mathbf{u}}, \tag{8}$$

is based on the volume averaged Navier-Stokes equations (Whitaker, 1996), and describes the bulk resistance to steady state flow of an incompressible fluid through porous material. This definition is based on the assumption that the pore space is completely filled by one phase. In a GDL partially saturated with liquid water, the pressure drop in the gas and liquid water phases are described by two adapted Darcy's equations each accounting with a relative permeability for the partial saturation

$$\nabla p_i = -\frac{\mu_i}{\mathbf{k}\mathbf{k}_{\mathbf{r},\mathbf{i}}}\bar{\mathbf{u}}_i. \tag{9}$$

The (relative) permeability of a fluid, $\mathbf{k}_{\mathbf{r},\mathbf{i}}$ and $\mathbf{k}$, can be determined based on the pore-scale velocity vector and pressure fields, by solving the mass and momentum conservation equations for each fluid phase (here, gas and liquid water),

$$\nabla \mathbf{u} = 0, \tag{10}$$

$$\mu \Delta \mathbf{u} = \nabla p, \tag{11}$$

assuming steady state, incompressible and Newtonian fluid conditions.

The relative permeability was determined by solving the mass and momentum conservation equations, Eqs. (10) and (11), on the pore-level for each fluid phase individually, assuming the other fluid phase to be stagnant. All of this was done for the various saturation levels. An in-house mesh generator was used for the spatial

discretization. The mesh generator uses the segmented CT data to construct a consistent 3D mesh of the individual fluid phases using tetrahedral mesh elements (Friess et al., 2013). GDL samples of sizes $780 \times 780 \times 260\ \mu m^3$ and $780 \times 780 \times 247\ \mu m^3$ for series A and series C, respectively, were used in the calculations. Each GDL sample was placed in a duct and the fluid phases were extended for an inlet and outlet domain of twice the sample thickness, 520 μm and 494 μm respectively, allowing the flow to develop. CFX 15 (2013), a commercial finite volume solver, was used for solving the steady state mass and momentum equations in each domain with zero velocity tangentially to the solid-fluid interface, periodic boundary condition at the lateral walls of the duct (*xz*- and *yz*-planes), uniform velocity at the inlet boundary (*xy*-planes at $z = 0$) and constant pressure at the outlet boundary (*xy*-planes at $z = z_{max}$). Mesh element numbers were in the range of several millions, typical mesh element sizes around 6.5—7 μm (mean values, the frequency peak of the mesh element size distribution lied at 4 μm), providing converged results with a reasonable computational expense, which is consistent with our previous studies (Haussener et al., 2012). The convergence criterion for the termination residual RMS of the iterative solution was set to 10^{-4} according to convergence studies. The calculated pressure drop in the pore-phase over the sample for Reynolds numbers equal to 0.01 and 0.1 were used to calculate the (relative) permeability, according to Eq. (9). Reynolds numbers are defined based on the mean pore diameter and superficial velocity. Example results of the pore level simulations are depicted in Fig. 3. Calculations for each Re number required four hours of computing time on a 2.3 GHz CPU workstation with 4 GB RAM. Relative permeability is often given as a functional of the gas occupied volume fraction or the saturation, respectively,

$$k_{r,gas} = (1 - s)^{\beta}, \tag{12}$$

$$k_{r,liquid} = s^{\lambda}, \tag{13}$$

with β and λ two constants. The effective (relative) gas diffusivity, D_{eff}, in liquid saturated porous media can be determined in analogy to the relative permeability, based on the pore-scale concentration field, and requires solving the mass conservation (Eq. (10)) and the species transport equation (Eq. (14)) in the two fluid phases,

$$\nabla(D\nabla c) = 0. \tag{14}$$

Macroscopically, the steady state stagnant species transport equation is given by (Weber et al., 2004),

$$\nabla(D_{eff}\nabla\bar{c}) = 0 \tag{15}$$

which is based on the volume averaged species transport equation, assuming that the species transport is considerable only in the gas phase and negligible in liquid phase (Whitaker, 1996). We assume steady state conditions and stagnant fluid flow ($\mathbf{u} = 0$). The effective (relative) gas diffusivity was determined by solving the mass and species transport equations (Eqs. (10) and (14)) on the pore-level in the gas phase. The same mesh and convergence criteria as for the fluid flow calculations were used. The same commercial finite volume solver was used for solving the steady state mass and species transport equations in the gas domain with impermeable gas-liquid and gas-solid interfaces, periodic boundary condition at the lateral walls of the duct, and given inlet and outlet concentrations. The calculated concentration gradient between inlet and outlet of the sample and the mass flux were used for the calculation of the effective gas diffusivity, according to Eqs. (14) and (15). Calculations for one saturation level required around one hour computing time on a 2.3 GHz CPU workstation with 4 GB RAM.

The flow paths of a pressure driven flow converge to concentration driven flux at very low Reynolds (Haussener et al., 2010). Hence, the velocity vector field of the permeability calculation at Reynolds equal 0.01 can be used for the calculation of tortuosity, defined by the ratio of length of flow streamline over sample thickness (Kaviany, 1991)

$$\tau = \frac{l_{path}}{l_{sample}}. \tag{16}$$

For each sample, more than a thousand streamlines with equally distributed starting points at the inlet were used to calculate the flow path tortuosity according to Eq. (16). Fig. 3 depicts an example of the pore-level calculations of the pressure and concentration fields and stream lines for the dry GDL case.

The directly calculated effective gas diffusivity will be fitted to correlations in which the ratio of the effective (relative) gas diffusivity and the bulk gas diffusivity are approximated by the product of two functions: one function solely dependent on the dry sample porosity, $f(\varepsilon)$, and one a function solely dependent on the saturation, $g(s)$, (Hwang and Weber, 2012; Kaviany, 1991; Nam and Kaviany, 2003; Rosén et al., 2012)

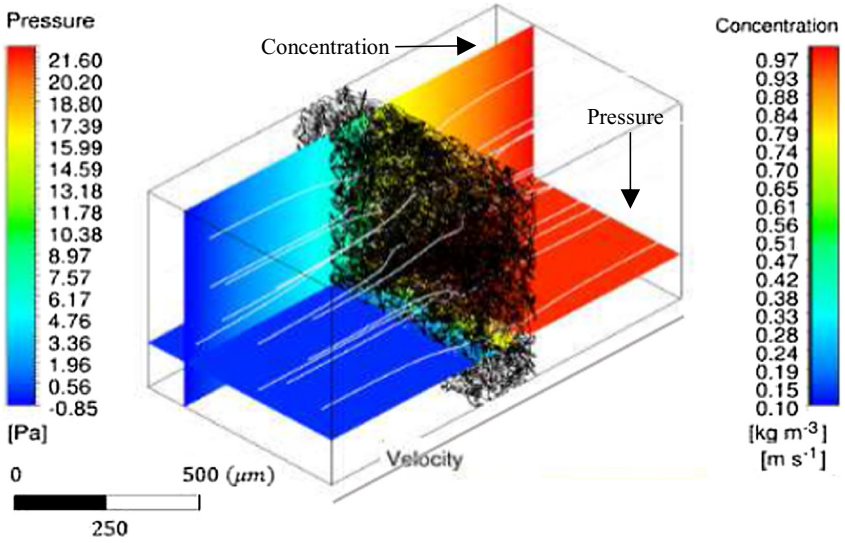

Fig. 3. An example of a visualization of the results of the direct pore-scale simulations. The simulated domain is the dry sample A at Reynolds equal to 0.01: pressure (horizontal plane) and concentration (vertical plane) fields, and streamlines indicating the tortuous flow path inside the GDL.

$$\frac{D_{\text{eff}}}{D} = f(\varepsilon)g(s). \tag{17}$$

The calculated tortuosity is used as an alternative method to determine the effective (relative) diffusivity according to (Martínez et al., 2009),

$$D_{\text{eff}} = \frac{\varepsilon^m}{\tau^k} D \tag{18}$$

by estimating the two lumped fitting parameters, m and k.

3. Results and discussion

The morphological characteristics of the GDL are presented as well as the transport characteristics. GDL show generally an anisotropic structure. Here we limit our investigations on the through-plane direction.

3.1. Morphological characterization

The samples' calculated gas phase volume fractions (i.e. porosities) are 0.70 and 0.68 for series A and series C, respectively. The trend of a slight reduction of porosity by adding PTFE is consistent with experimental observations (Hwang and Weber, 2012). Our calculated values are in good agreement with the values reported for Toray-TGP-H-120 papers, slightly below the values reported by Hussaini et al. of 0.72 for sample A measured by liquid saturation (Hussaini and Wang, 2010), by Lobato et al. of 0.76 for sample A and 0.74 for sample C measured by mercury porosimetry (Lobato et al., 2008), and 0.76 and 0.73 by the buoyancy technique (Rashapov et al., 2015). It is known that the surface regions have higher porosity than the core of the GDL. Thus, trimming the outer layers of the experimental sample, we expected the calculated porosity to be lower than the reported bulk experimental measurements.

Calculated saturation of the pore volume with increasing capillary pressure shows agreement with trends seen in the experimental data of Gostick et al. (Gostick et al., 2009) (Fig. 4). By increasing the capillary pressure, the percolating phase (water) invades the pores, first the pores with larger diameters than the ones with smaller diameters. This process is hindered by the partially hydrophobic fiber surfaces in sample C. Therefore at the same capillary pressures, sample C has relatively lower saturation in comparison to sample A. The discrepancies between the curves is likely due to inhomogeneity of the saturation in the boundaries of the experimental sample (García-Salaberri et al., 2015a).

The phase size distribution of fiber and pore space of the dry sample A and C are depicted in Fig. 5. The mean diameters of the fiber and pore phases are 16.3 μm and 30.5 μm, respectively. The calculated data does not show any significant difference between the dry samples A and C.

The gas phase size distribution of samples A and C are plotted in Fig. 6(a) and (c). It demonstrates that the mean size non-linearly shifts from 30.1 μm to 10.6 μm (sample A) and 30.9 μm to 11.5 μm (sample C) when increasing the capillary pressure from 0 to 6000 Pa (sample A) and 0–8000 Pa (sample C), respectively (Fig. 7). The shifts to smaller sizes with increasing capillary pressure is a result of the liquid water intrusion into the pores, starting at the largest pores first and accessing progressively smaller pores with increasing capillary pressure. We observe a difference between the untreated and the PTFE treated samples, specifically at low saturations: the addition of PTFE rejects water from smaller pores, hinders a complete filling of the larger pore spaces, and generally requires larger capillary pressures to reach the same saturation as in sample A. At high saturations, i.e. high capillary pressures, the liquid phase fills all the pores and its size distribution follows the pore shape of the material.

The liquid water size distributions at different capillary pressures for samples A and C are depicted in Fig. 6(b) and (d). Small water clusters started to evolve in the larger pore space (usually starting in the corners of fiber intersections) and grew until the large pores were filled. We noted that there are small artefacts in the water phase from the phase segmentation, contributing to the 5 μm-peak. This contribution is more significant at lower saturations where a smaller amount of water clusters is present. The mean diameter of the liquid water phase size distribution of series A samples shifts from 9.8 μm to 30.6 μm increasing the capillary pressure from 1000 to 6000 Pa (Fig. 7). The mean diameter of the liquid water phase size distribution of series C samples shifts from 5.9 μm to 31.1 μm increasing the capillary pressure from 1000 to 8000 Pa (Fig. 7). A small reduction in mean diameter of the liquid water phase size distribution at intermediate saturations (0.4–0.7) shows that the large pores were filled before the small ones, which started to be accessible at these intermediate saturations. A small difference between the untreated and the PTFE treated sample is observed only initially (i.e. at low capillary pressures and saturations smaller than 0.1) where smaller liquid water sizes are observed as the PTFE hinders a complete filling of the larger pore spaces (see also percolation discussion below). At large capil-

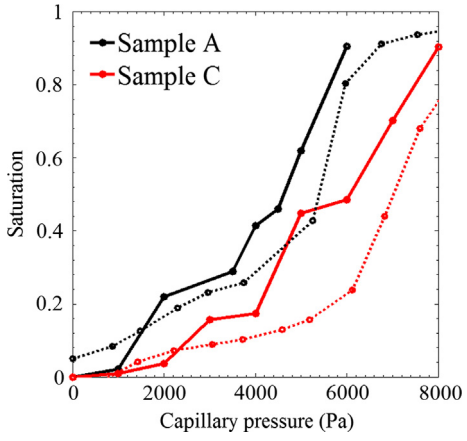

Fig. 4. Calculated saturation for various capillary pressures for sample A (solid, black) and sample C (solid, red), and experimentally measured saturation (dotted) during primary injection for series A (dotted, black) and C (dotted, red) without compression by Gostick et al. (2009). (For interpretation of the references to color in this figure legend, the reader is referred to the web version of this article.)

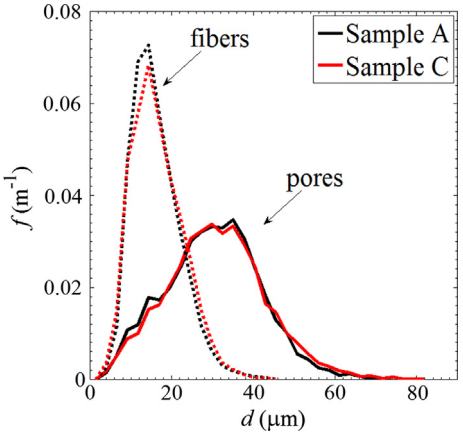

Fig. 5. The phase size distributions of the fibers (dotted) and pores (solid) of dry sample A (black) and sample C (red). (For interpretation of the references to color in this figure legend, the reader is referred to the web version of this article.)

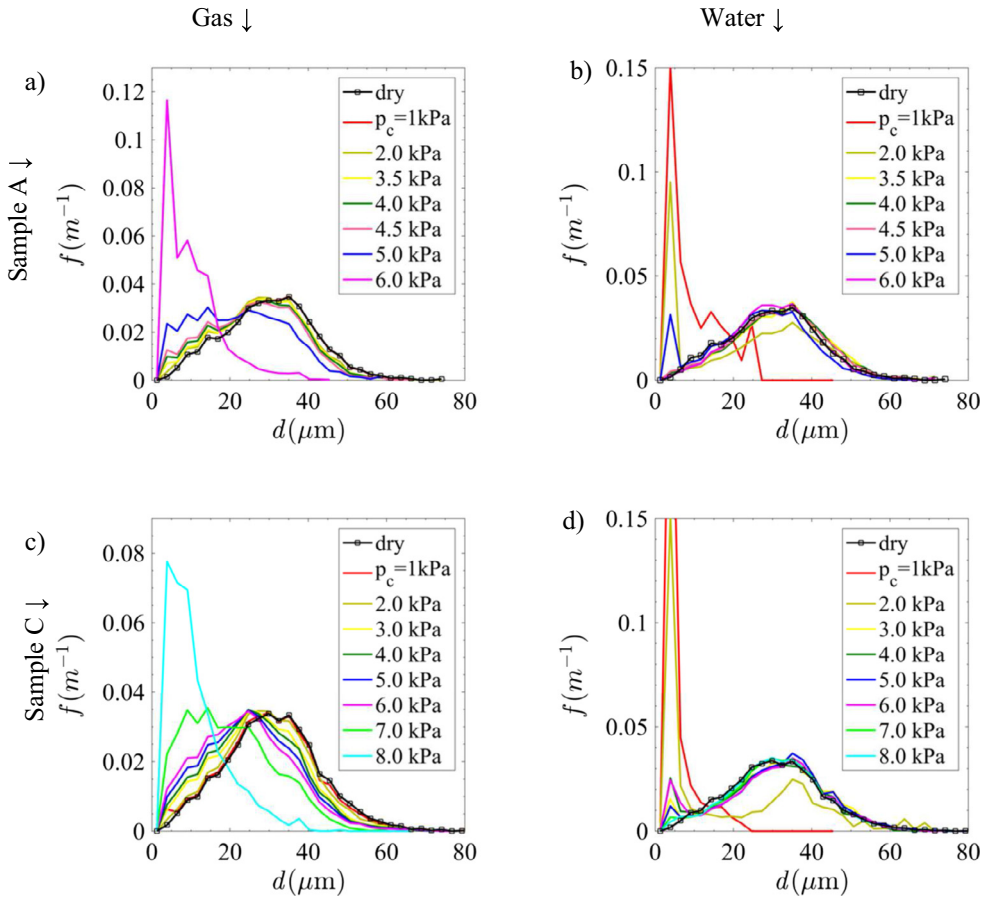

Fig. 6. Gas phase (a and c) and liquid water phase (b and d) size distributions for varying capillary pressures of sample A (a and b) and C (c and d), respectively. Increasing capillary pressure leads to higher saturation, and hence shifts the phase size distribution toward smaller and larger diameters for gas and liquid water, respectively.

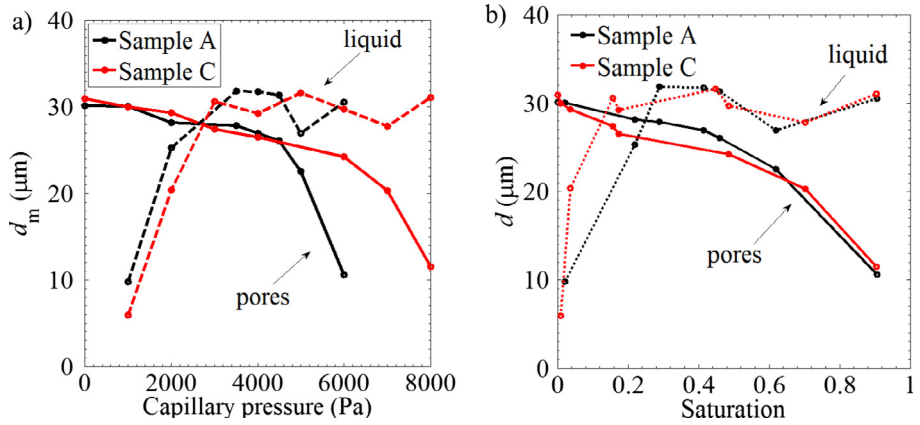

Fig. 7. Mean diameter of pore (solid lines) and liquid (dashed lines) phase size distribution as a function of a) capillary pressure and b) saturation, for sample A (black) and sample C (red). (For interpretation of the references to color in this figure legend, the reader is referred to the web version of this article.)

lary pressures, the liquid water size converges to the typical empty pore space dimension for both sample types.

3.2. Permeability

The calculated through-plane permeability for the Toray series A and series C samples was $9.36 \cdot 10^{-12}$ m^2 and $5.79 \cdot 10^{-12}$ m^2, respectively. These values compare well to experimentally measured permeabilities. Lobato et al. experimentally determined the permeability to be $9.21 \cdot 10^{-12}$ m^2 and $7.77 \cdot 10^{-12}$ m^2 for series A and series C, respectively (Lobato et al., 2008). Hussaini and Wang (2010) and Williams et al. (2004) measured $8.59 \cdot 10^{-12}$ m^2 and $14.7 \cdot 10^{-12}$ m^2 for the series A. Semi-empirical permeability models such as the permeability assuming Hagen-Poisseuille flow in a channel of $19.82 \cdot 10^{-12}$ m^2, and the Carman-Kozeny model-based permeability of $19.18 \cdot 10^{-12}$ m^2 provide fair estimate for permeability of the system.

The air and water relative through-plane permeabilities are depicted in Fig. 8a together with the best fit for the expressions given in Eqs. (12) and (13) for each phase. The best fit parameters

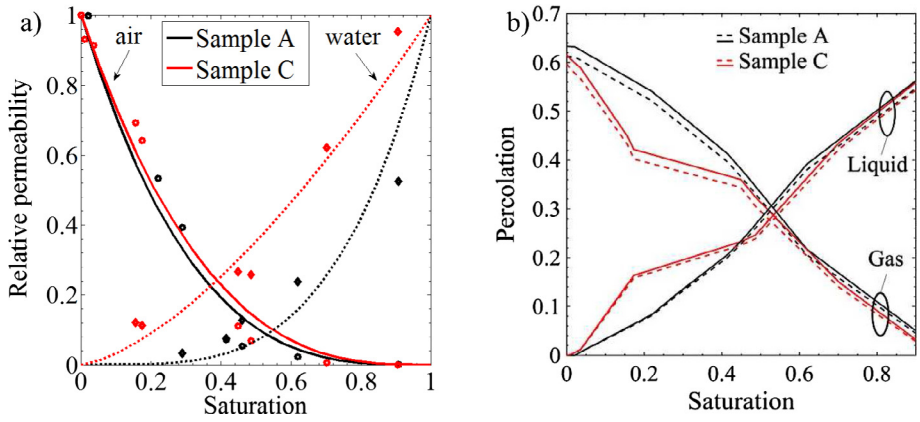

Fig. 8. (a) Gas (solid lines) and liquid water (dotted lines) relative through-plane permeability (dots) and best fits (lines). (b) Percolation analysis of both samples in through-plane direction (dashed lines) and average 3D (solid lines). Sample A (black) and sample C (red). (For interpretation of the references to color in this figure legend, the reader is referred to the web version of this article.)

obtained by a least-square fitting are given in table 1. The predicted fitting values are in the range of what has been reported by Rosén et al. in their numerical study, namely $\beta = 3$ for a Toray TGP-H-060 sample with 20% PTFE loading (Rosén et al., 2012), and Zamel et al. proposed $\beta = \lambda = 3.5$ for general carbon paper (Zamel et al., 2011).

Comparing the relative permeability of the two samples demonstrate that the PTFE treated sample provide higher liquid water permeability at the same saturation. The largest differences between the two samples are in the range of 40% at a saturation of 0.45. This result suggests that adding PTFE facilitates water transport along the primary transport axis, hindering the spread of water in the perpendicular directions. In other words, the PTFE treatment drives liquid water to be more selective on the pore diameter anisotropy and develops preferentially in through-plane direction. To examine this hypothesis, we performed percolation analysis of the air and liquid water phases inside the pore space of both samples in through plane direction. Fig. 8b demonstrates that water percolates better in sample C at low saturations (between 0.05 and 0.45). This larger percolation indicates that the water channels better developed in through-plane direction. For high saturation, water occupies all pores and both sample converge to the same percolation, as expected.

3.3. Effective gas diffusivity

The effective through-plane gas diffusivity of the dry sample A and C are 0.35 and 0.28, respectively, normalized by the bulk gas phase diffusivity. This term is equivalent to the $f(\varepsilon)$ function in Eq. (17). As observed (Rosén et al., 2012), adding PTFE-coating is reducing porosity which results in reducing effective diffusivity in dry sample since $f(\varepsilon)$ is a decreasing function of porosity. The two values obtained for $f(\varepsilon)$ in the range experimentally measured by Hwang and Weber (Hwang and Weber, 2012), and LaManna and Kandlikar (LaManna and Kandlikar, 2011).

The calculated relative effective gas diffusivity for various liquid saturations of sample A and sample C are depicted in Fig.9a. Increasing saturation restricts the gas flux (as the liquid phase is impermeable to water) and increases the tortuosity by reducing the gas phase volume domain which result in reducing relative gas diffusivity (Fig. 10). Here, we observed only minor changes in the relative effective gas diffusivity when treating the GDL with PTFE. Typically, the $g(s)$ function in Eq. (17) is fitted to two different types of functions, given by:

$$g(s) = (1 - s)^{\alpha} \tag{19}$$

$$g(s) = \frac{1}{2}\left[1 + \mathrm{erf}\left(-\frac{\ln(s) + a}{b}\right)\right], \tag{20}$$

where the latter has been proposed for GDL with hydrophobic coating (Hwang and Weber, 2012). A least-square fit of the calculated data to Eq. (19) predicted $\alpha = 3.05$ for series A samples and $\alpha = 2.75$ for series C samples (Table 1). These values compare well with experimentally determined values $\alpha \approx 3$ (Hwang and Weber, 2012; Rosén et al., 2012). Adding PTFE slightly reduces the effect of saturation on diffusivity, the effective diffusivity reduces slower with increasing saturation ($\alpha = 3.05$ for sample C in comparison to $\alpha = 2.75$ for sample A). A least-square fit of the calculated data of sample C to Eq. (20) predicted $a = 1.55$ and $b = 0.99$ (Table 1). These values compare reasonably with experimentally determined values by Hwang et al. of $a = 1.27$ and $b = 0.82$ (Hwang and Weber, 2012). Looking at the detailed comparison between our calculated values of sample C and the experimental data of Hwang et al. reveals however that our calculations predict a sharper drop in $g(s)$ with increasing s, potentially explained by the observed inhomogeneity of the water distribution in the sample (García-Salaberri et al., 2015b).

The distribution of tortuosity directly calculated from streamlines for sample A and C at different saturations are depicted in Fig. 10. The tortuosity distribution of both samples shifts towards

Table 1
Fitting parameter for relative gas and liquid permeability, Eqs. (12) and (13), and for relative effective gas diffusivity, Eqs. (19) and (20). Eq. (20) was proposed for GDL with hydrophobic coatings and is only applicable to sample C.

	Equation	Parameter	Sample A	R^2 for A	Sample C	R^2 for C
Permeability for dry sample	–	–	$9.36 \cdot 10^{-12}$ m^2	–	–	$5.79 \cdot 10^{-12}$ m^2
Rel. gas permeability	(12)	β	3.24	0.97	2.90	0.98
Rel. liquid permeability	(13)	λ	3.87	0.82	1.50	0.97
Rel. eff. gas diffusivity	(19)	α	3.05	0.99	2.75	0.99
Rel. eff. gas diffusivity	(20)	a, b	–	–	1.55, 0.99	0.99

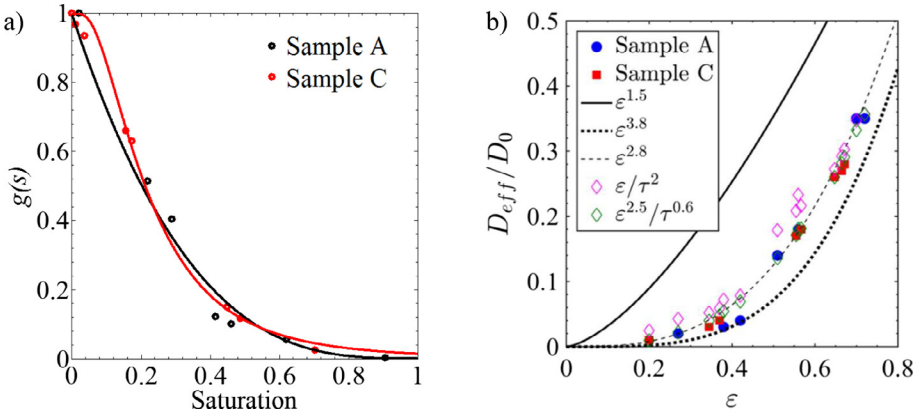

Fig. 9. (a) Directly calculated relative effective through-plane gas diffusivity as a function of saturation for sample A (black circle) and sample C (red circle), best fit of Eq. (19) for sample A with $\alpha = 3.05$, and of Eq. (20) for sample C with $a = 1.55$ and $b = 0.99$. (b) Calculated effective relative through-plane gas diffusivity as a function of porosity (i.e. gas phase volume fraction). The best fits to our data $\varepsilon^{2.8}$, and $\varepsilon^{2.5}/\tau^{0.6}$ as best fit to directly calculated tortuosity (its mean value), are compared with known equations proposed in literature, Bruggeman $\varepsilon^{1.5}$, Martinez et al. $\varepsilon^{3.8}$ (Martínez et al., 2009), and Epstein ε/τ^2 (Epstein, 1989).

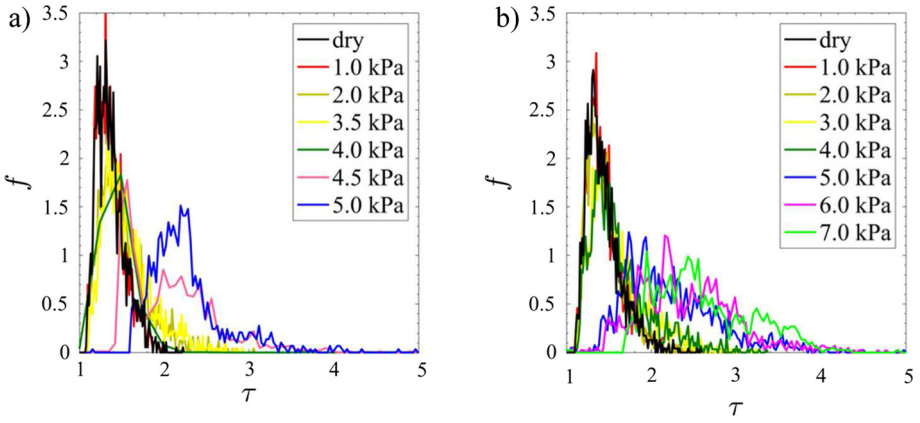

Fig. 10. Distribution of tortuosity of streamlines in sample A (a) and sample C (b), for varying capillary pressures.

larger tortuosities with increasing applied capillary pressure, and the distribution shape becomes wider. The major change happens for $p_c > 4$ kPa. Both samples show the same transition of the tortuosity distribution with increasing applied capillary pressure. However, the mean tortuosity of sample A is slightly lower than that for sample C at the same gas phase volume fraction (Fig. 11). Here, gas phase volume fraction can be seen as porosity since the liquid phase assumed to be stagnant and was treated as GDL fiber in the simulation.

The relative effective gas diffusivity can be directly related to porosity and tortuosity. Knowing the tortuosity from the simulation permits evaluation of the validity of the reported relations in literature and even propose a specific relation for GDLs. Optimizing the two exponents of Eq. (18) to relate effective diffusivity to tortuosity and porosity leads to $m = 2.5$ and $k = 0.6$ ($R^2 = 0.99$) (Fig. 9b).

Conventionally, tortuosity has been estimated by using expressions relating effective diffusivity to porosity and tortuosity. The best fit of such relations to our data requires $\varepsilon^{2.8}$ (Fig. 9b). The relation reported by Martínez et al. (2009) shows to be a lower bound for our data ($\varepsilon^{3.8}$ in Fig. 9b), while, the Brugmann equation overestimates significantly the effective diffusivity. A popular set of exponents for Eq. (18) is $k = 1$ and $m = 2$ (Epstein's equation) (Epstein, 1989). Combining the best fit to this set of exponents leads to $\tau_{mean} = \varepsilon^{-0.9}$, reasonably relating porosity and tortuosity particularly at high porosities (Fig. 11). However, this relation

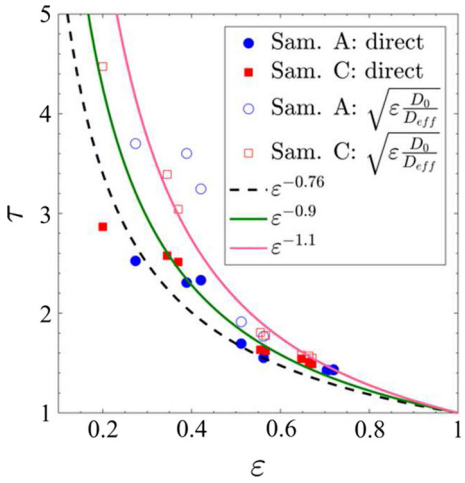

Fig. 11. Directly calculated tortuosity as a function of gas phase volume fraction (filled symbols), and indirectly calculated tortuosity via the Epstein's equation diffusivity calculations (Eq. (18) with $k = 1$ and $m = 2$, hollow symbols). Porosity-dependent fits (solid and dashed lines) with $\varepsilon^{-0.76}$ providing the best fit for the directly calculated tortuosity.

slightly overestimates tortuosity in comparison to the best fit ($m = 2.5$ and $k = 0.6$) to the tortuosity porosity data, which is $\tau_{mean} = \varepsilon^{-0.76}$.

4. Conclusion

3D microstructures obtained from high resolution CT-imaging were used in direct pore-level numerical flow simulation to investigate morphological characteristics and effective saturation dependent transport properties of common gas diffusion media of PEMFCs, specifically focusing on the difference between untreated and PTFE-loaded GDLs (Toray TGP-H-120, with and without PTFE loading). An advanced tomography data post-processing was used to accurately segment the gas, liquid water, and solid fiber phases. The post-processing consisted of anisotropic diffusion filters and manual histogram-based thresholding of the fibers and the other two phases. The segmented dry sample was then accurately aligned with the partially saturated samples, and the fibers removed. Closing and median filter where used to remove fragments, before a second manual histogram-based thresholding of the gas and liquid water phase was achieved. The sensitivity of the calculated morphological and transport characteristics on the thresholding was within reasonable thresholds (±5% variation in the two thresholding values resulted in $\lessapprox$±5% variations in the properties) and provided confidence in the segmentation approach.

The morphological characterization of the untreated (sample A) and PTFE-treated samples (sample C) provided the basis for the interpretation of the transport characteristics. Specifically, size distributions of the gas, liquid water, and fiber phases were calculated at different applied capillary pressures utilizing mathematical morphology operations. These calculations showed that the gas phase size distribution shifted to smaller diameters with increasing saturation, although significantly less steep in the PTFE-treated sample compared to the untreated one. Conversely, the liquid water size distribution shifted to higher diameters with increasing capillary pressure, however a less significant difference between sample A and C was observed.

The calculated through-plane gas relative permeability decreased with increasing saturation while the liquid water relative permeability increased with saturation. A pronounced difference in the relative water permeability between the two samples was observed. The power law exponent was fitted to the data and an exponent of around 1.5 was found for hydrophobic treated sample, namely sample C, while for the GDL without hydrophobic treatment it was found to be around 3. This shows the importance of optimal PTFE loading in enhancing water management in GDLs. To investigate the underlying phenomena causing this difference, percolation analysis was carried out to show how the liquid water phase is distributed in the pores of both samples. It demonstrated that water percolates better in sample C than A at the same saturations (particularly valid at low to intermediate saturations). A better percolation of water in sample C leads to preferential and percolating flow channels for water transport. Thus, water permeability not only is a function of saturation but also depends on water percolation through the sample. Moreover, relative effective gas diffusivity of the two samples were calculated and compared. Power law expression were fitted with exponents of around 3 for these properties for both samples. No significant difference was observed between the two samples. However, it is worth noting that at a fixed capillary pressure, sample C has lower saturation, and hence, its pores are less blocked, providing better reactant transport.

Finite volume method used in this study permits direct calculation of tortuosity. Calculated tortuosity distributions shifted to larger values with increasing saturation, and the distribution function widened. Through-plane relative effective diffusivity for both samples were calculated. These results were used to examine the validity of the known correlation between effective diffusivity, porosity and tortuosity. Tortuosity-dependent prediction of the diffusivity fitted well when the exponents of the porosity and tortuosity in Eq. (18) were individually adapted. The expression proposed by Epstein (Epstein, 1989) provided an accurate correlation between the three parameters, particularly at high porosities. The Bruggeman expression over predicted the relative effective diffusivity, while, the expression from Martínez et al. (2009) can serve as lower bound of our data.

Our investigation demonstrates that adding PTFE reduces the porosity of the GDL, significantly slows the reduction in gas phase size distribution with increasing saturation, and significantly increases the relative liquid water permeability and help to construct a better liquid percolation. This investigation helps to understand the transport properties of gas diffusion media more precisely, and specifically provide insights on the effect of PTFE loading on the transport opening pathways for GDL optimization.

Acknowledgment

The authors thank Ezequiel Medici from MTU and Sarah Van Rooij from EPFL for fruitful discussions. We thank the Swiss National Science Foundation for the partial funding under grant #200021_169913.

Author contributions

S.H. designed the project. S.H. and S.M.M. performed calculations and interpreted the results. M.N. performed sensitivity studies. S.H. implemented the morphological codes. J.G. performed experiments and analyzed experimental data. All authors contributed in writing the manuscript.

References

ANSYS CFX 15. Ansys Inc., 2013.
Bear, J., Bachmat, Y., 1990. Introduction to Modeling of Transport Phenomena in Porous Media. Springer.
Berryman, J.G., Blair, S.C., 1986. Use of digital image analysis to estimate fluid permeability of porous materials: application of two-point correlation functions. J. Appl. Phys. 60, 1930–1938.
Chan, C., Zamel, N., Li, X., Shen, J., 2012. Experimental measurement of effective diffusion coefficient of gas diffusion layer/microporous layer in PEM fuel cells. Electrochim. Acta 65, 13–21.
Darcy, H., 1856. Les fontaines publiques de la ville de Dijon.
Epstein, N., 1989. On tortuosity and the tortuosity factor in flow and diffusion through porous media. Chem. Eng. Sci. 44, 777–779.
Fishman, Z., Bazylak, A., 2011. Heterogeneous through-plane porosity distributions for treated PEMFC GDLs I. PTFE effect. J. Electrochem. Soc. 158, B841–B845.
Flückiger, R., Freunberger, S.A., Kramer, D., Wokaun, A., Scherer, G.G., Büchi, F.N., 2008. Anisotropic, effective diffusivity of porous gas diffusion layer materials for PEFC. Electrochim. Acta 54, 551–559.
Flückiger, R., Marone, F., Stampanoni, M., Wokaun, A., Büchi, F.N., 2011. Investigation of liquid water in gas diffusion layers of polymer electrolyte fuel cells using X-ray tomographic microscopy. Electrochim. Acta 56, 2254–2262.
Friess, H., Haussener, S., Steinfeld, A., Petrasch, J., 2013. Tetrahedral mesh generation based on space indicator functions. Int. J. Numer. Meth. Eng. 93, 1040–1056.
García-Salaberri, P.A., Gostick, J.T., Hwang, G., Weber, A.Z., Vera, M., 2015a. Effective diffusivity in partially-saturated carbon-fiber gas diffusion layers: effect of local saturation and application to macroscopic continuum models. J. Power Sources 296, 440–453.
García-Salaberri, P.A., Hwang, G., Vera, M., Weber, A.Z., Gostick, J.T., 2015b. Effective diffusivity in partially-saturated carbon-fiber gas diffusion layers: effect of through-plane saturation distribution. Int. J. Heat Mass Transf. 86, 319–333.
Ghanbarian, B., Cheng, P., 2016. Application of continuum percolation theory for modeling single-and two-phase characteristics of anisotropic carbon paper gas diffusion layers. J. Power Sources 307, 613–623.
Gonzalez, R.C., Woods, R.E., 2002. Digital Image Processing. Prentice Hall Upper Saddle River, NJ.
Gostick, J.T., Ioannidis, M.A., Fowler, M.W., Pritzker, M.D., 2007. Pore network modeling of fibrous gas diffusion layers for polymer electrolyte membrane fuel cells. J. Power Sources 173, 277–290.
Gostick, J.T., Ioannidis, M.A., Fowler, M.W., Pritzker, M.D., 2009. Wettability and capillary behavior of fibrous gas diffusion media for polymer electrolyte membrane fuel cells. J. Power Sources 194, 433–444.

Haralick, R.M., Sternberg, S.R., Zhuang, X., 1987. Image Analysis Using Mathematical Morphology. Pattern Analysis and Machine Intelligence, IEEE Transactions on PAMI-9, 532–550.
Haussener, S., Coray, P., LipiÍ, W., Wyss, P., Steinfeld, A., 2010. Tomography-based heat and mass transfer characterization of reticulate porous ceramics for high-temperature processing. J. Heat Transf. 132, 023305.
Haussener, S., Jerjen, I., Wyss, P., Steinfeld, A., 2012. Tomography-based determination of effective transport properties for reacting porous media. J. Heat Transf. 134, 012601.
Hilfer, R., 1996. Transport and relaxation phenomena in porous media. Adv. Chem. Phys. 92, 299–424.
Hilpert, M., Miller, C.T., 2001. Pore-morphology-based simulation of drainage in totally wetting porous media. Adv. Water Resour. 24, 243–255.
Hussaini, I., Wang, C., 2010. Measurement of relative permeability of fuel cell diffusion media. J. Power Sources 195, 3830–3840.
Hwang, G., Weber, A., 2012. Effective-diffusivity measurement of partially-saturated fuel-cell gas-diffusion layers. J. Electrochem. Soc. 159, F683–F692.
Ismail, M., Ingham, D., Hughes, K., Ma, L., Pourkashanian, M., 2015. Effective diffusivity of polymer electrolyte fuel cell gas diffusion layers: an overview and numerical study. Int. J. Hydrogen Energy 40, 10994–11010.
Jain, A.K., 1989. Fundamentals of Digital Image Processing. Prentice-Hall Inc.
Kaestner, A., Lehmann, E., Stampanoni, M., 2008. Imaging and image processing in porous media research. Adv. Water Resour. 31, 1174–1187.
Kaviany, M., 1991. Principles of Heat Transfer in Porous Media. Springer, Principles of Heat Transfer in Porous Media.
Koido, T., Furusawa, T., Moriyama, K., 2008. An approach to modeling two-phase transport in the gas diffusion layer of a proton exchange membrane fuel cell. J. Power Sources 175, 127–136.
Kramer, D., Freunberger, S.A., Flückiger, R., Schneider, I.A., Wokaun, A., Büchi, F.N., Scherer, G.G., 2008. Electrochemical diffusimetry of fuel cell gas diffusion layers. J. Electroanal. Chem. 612, 63–77.
Kumar, R.J.F., Radhakrishnan, V., Haridoss, P., 2012. Enhanced mechanical and electrochemical durability of multistage PTFE treated gas diffusion layers for proton exchange membrane fuel cells. Int. J. Hydrogen Energy 37, 10830–10835.
LaManna, J.M., Kandlikar, S.G., 2011. Determination of effective water vapor diffusion coefficient in pemfc gas diffusion layers. Int. J. Hydrogen Energy 36, 5021–5029.
Larminie, J., Dicks, A., McDonald, M.S., 2003. Fuel Cell Systems Explained. Wiley, New York.
Lobato, J., Cañizares, P., Rodrigo, M., Ruiz-López, C., Linares, J., 2008. Influence of the Teflon loading in the gas diffusion layer of PBI-based PEM fuel cells. J. Appl. Electrochem. 38, 793–802.
Martínez, M.J., Shimpalee, S., Van Zee, J., 2009. Measurement of MacMullin numbers for PEMFC gas-diffusion media. J. Electrochem. Soc. 156, B80–B85.
Nam, J.H., Kaviany, M., 2003. Effective diffusivity and water-saturation distribution in single-and two-layer PEMFC diffusion medium. Int. J. Heat Mass Transf. 46, 4595–4611.
Nguyen, T., Lin, G., Ohn, H., Hussey, D., Jacobson, D., Arif, M., 2006. Measurements of two-phase flow properties of the porous media used in PEM fuel cells. ECS Trans. 3, 415–423.
Park, J., Oh, H., Ha, T., Lee, Y.I., Min, K., 2015. A review of the gas diffusion layer in proton exchange membrane fuel cells: durability and degradation. Appl. Energy 155, 866–880.
Perona, P., Malik, J., 1990. Scale-space and edge detection using anisotropic diffusion. IEEE Trans. Pattern Anal. Mach. Intell. 12, 629–639.
Petrasch, J., Wyss, P., Stämpfli, R., Steinfeld, A., 2008. Tomography-based multiscale analyses of the 3D geometrical morphology of reticulated porous ceramics. J. Am. Ceram. Soc. 91, 2659–2665.
Prodanović, M., Bryant, S.L., 2006. A level set method for determining critical curvatures for drainage and imbibition. J. Colloid Interface Sci. 304, 442–458.
Rashapov, R.R., Gostick, J.T., 2016. In-plane effective diffusivity in PEMFC gas diffusion layers. Transp. Porous Media, 1–23.
Rashapov, R.R., Unno, J., Gostick, J.T., 2015. Characterization of PEMFC gas diffusion layer porosity. J. Electrochem. Soc. 162, F603–F612.
Rosén, T., Eller, J., Kang, J., Prasianakis, N.I., Mantzaras, J., Büchi, F.N., 2012. Saturation dependent effective transport properties of PEFC gas diffusion layers. J. Electrochem. Soc. 159, F536–F544.
Sole, J.D., 2008. Investigation of Water Transport Parameters and Processes in the Gas Diffusion Layer of PEM Fuel Cells PhD Dissertation. Virginia Polytechnic Institute and State University. PhD dissertation.
Suter, S., Steinfeld, A., Haussener, S., 2014. Pore-level engineering of macroporous media for increased performance of solar-driven thermochemical fuel processing. Int. J. Heat Mass Transf. 78, 688–698.
Utaka, Y., Tasaki, Y., Wang, S., Ishiji, T., Uchikoshi, S., 2009. Method of measuring oxygen diffusivity in microporous media. Int. J. Heat Mass Transf. 52, 3685–3692.
Wang, C.-Y., 2004. Fundamental models for fuel cell engineering. Chem. Rev. 104, 4727–4766.
Weber, A.Z., Darling, R.M., Newman, J., 2004. Modeling two-phase behavior in PEFCs. J. Electrochem. Soc. 151, A1715–A1727.
Weber, A.Z., Newman, J., 2004. Modeling transport in polymer-electrolyte fuel cells. Chem. Rev. 104, 4679–4726.
Weszka, J.S., 1978. A survey of threshold selection techniques. Comput. Graph. Image Process. 7, 259–265.
Whitaker, S., 1996. The Forchheimer equation: a theoretical development. Transp. Porous Media 25, 27–61.
Whitaker, S., 1999. The Method of Volume Averaging. Theory and Applications of Transport in Porous Media. Kluwer Academic Publishers, Dordrecht. Cited on page (s) 60, 61–62.
Wildenschild, D., Sheppard, A.P., 2013. X-ray imaging and analysis techniques for quantifying pore-scale structure and processes in subsurface porous medium systems. Adv. Water Resour. 51, 217–246.
Williams, M.V., Begg, E., Bonville, L., Kunz, H.R., Fenton, J.M., 2004. Characterization of gas diffusion layers for PEMFC. J. Electrochem. Soc. 151, A1173–A1180.
Yu, S., Li, X., Liu, S., Hao, J., Shao, Z., Yi, B., 2014. Study on hydrophobicity loss of the gas diffusion layer in PEMFCs by electrochemical oxidation. RSC Adv 4, 3852–3856.
Zamel, N., Li, X., 2013. Effective transport properties for polymer electrolyte membrane fuel cells–with a focus on the gas diffusion layer. Prog. Energy Combust. Sci. 39, 111–146.
Zamel, N., Li, X., Becker, J., Wiegmann, A., 2011. Effect of liquid water on transport properties of the gas diffusion layer of polymer electrolyte membrane fuel cells. Int. J. Hydrogen Energy 36, 5466–5478.